

An Algorithm for Physics Informed Scan Path Optimization in Additive Manufacturing

B. Stump^{1,2}

¹Materials Science and Technology Division, Oak Ridge National Laboratory, Oak Ridge, TN

²Manufacturing Demonstration Facility, Oak Ridge National Laboratory, Knoxville, TN

Abstract

Site specific microstructure control is a critical research area within the field of additive manufacturing due to its potential to revolutionize part performance. One way to achieve site specific microstructure control is through control of the solidification conditions via the construction of intricate scan paths; however, the search space for such a problem is large. Previous attempts only considered the solidification conditions at the top surface while also requiring either lots of manual-fine tuning or large amounts of computational resources. This paper introduces a general method for scan path optimization which considers the solidification conditions in the bulk of the material without an increase in computational expense. This method consists of three core components:

1. A heat transfer model for simulating the temperature field at a given time.
2. A surrogate model which takes scan pattern information and temperature data and predicts the solidification conditions of the bulk as well as the meltpool depths for a spot melt.
3. A decision algorithm to decide which spot melt should be printed next based on the outputs of the surrogate model.

Each of these components can be changed without changing the overall method. Within this paper, this method is applied in the creation of an algorithm containing a semi-analytic heat transfer model to simulate the temperature field, a fully convolutional neural network (FCNN) as the surrogate model, and a greedy decision algorithm. The resulting algorithm produced complex scan patterns which gave strong results for simulated microstructure control.

Keywords: Additive Manufacturing, Microstructure Control, Scan Path Optimization, Numerical Modeling, Machine Learning

1. Introduction

Additive manufacturing offers the promise of unprecedented levels of control in both the design and performance of parts. Within the field of additive manufacturing, there have been many parallel approaches for fabricating parts, such as directed energy deposition (DED) and powder bed fusion (PBF). DED process involves using a heat source, either laser or electron beam, to melt material which comes from a moving nozzle [1]. In PBF processes, a layer of powder is deposited before being selective melted by either a laser (L-PBF) or electron beam (E-PBF). DED processes have both a higher build rate and lower production cost; however, they lack the potential for massive control of the thermal profile throughout the design process. The increase in thermal control PBF processes offer is because the speed at which an

electron beam or laser can move across a plane is many orders of magnitude faster than a nozzle which deposits mass. For these reasons, each approach is valid for different applications but this paper, whose focus is on fine control of the thermal conditions, focuses on PBF.

Having a large degree of control over the thermal conditions experienced by a part is a major goal of PBF processing since the macroscopic material properties of additively manufactured metals are largely determined by their microstructure [2] which is, in turn, determined by these thermal conditions [1,3]. If the thermal conditions can be fully controlled, it is possible to have site-specific control over microstructure thus enabling different regions of a part to have their microstructures directly tailored to the functional needs of the part, whether structural [4] or electromagnetic [5]. Microstructure is a broad term and in the context of additive manufacture, can include grain size and morphology [6,7], crystallographic texture [8–11], dendrite arm spacing [12], defect formation [13,14], and the various phases present [15,16]. Additionally, quantifying differences between various microstructures is not simple and many different approaches have sought to tackle this problem including complex spatial statistics [17] and machine learning [18].

When attempting microstructure control, it is common to simplify the problem by only considering the overall morphology of the grains which can broadly be classified as either equiaxed grains or columnar grains with the formation of each being closely related to the solidification gradient and velocity [19,20]. The solidification gradient and velocity are two parameters which describe the thermal field at a point in space as it is transitioning from liquid to solid. These parameters cannot be directly observed, although there have been attempts at indirectly observing them via in-situ monitoring [4], but can be simulated using a variety of frameworks. These computational frameworks include material point method (MPM) [21], finite element method (FEM) [22–24], finite volume method (FVM) [25], and analytic models [26–28]. When choosing which framework to use, the tradeoff between speed and accuracy must be considered. Resolving the free surface, individual particles, and the ray traced path of a heat source allows for a deeper understanding of the underlying physics; however, such models are often limited to only simulating domains of a few millimeters. Neglecting all physical phenomena except heat conduction reduces the accuracy of the simulation but improves the speed by several orders of magnitude. The quickest of these solutions are the analytic models which also offer several algorithmic advantages, such as not needing to simulate an entire domain [29].

There has been some success in controlling the microstructure by varying the processing parameters associated with raster patterns [30–32]. These processing parameters include hatch spacing, beam velocity, beam power, rotation between layers, and even beam shape. Another, more complicated approach has been to alter the scan strategy itself [8,33,34]. Changing the scan strategy utilizes the flexibility of E-PBF scanning systems but the problem itself is very complex. Early attempts at advanced scan pattern generation involve the hand-crafting of a new, general scan strategies where the parameters can be adjusted in an attempt to alter the microstructure [8,33]. These scan strategies are then simulated after a build is completed to discover underlying relationships or validate the models. A recent, general attempt, involved utilizing an analytic heat transfer model to output the solidification conditions which informs the cost function of a genetic algorithm [34]. The genetic algorithm implementation took many iterations to converge thus requiring large amounts of computational

resources despite only considering the top surface; however, creating a general, purely computational approach is a step in the right directions since it not only takes out the manual fine-tuning, but can also give much more complex scan patterns. The goal of this paper is to introduce a new general, purely computational method for the construction of advanced scan patterns which can consider the bulk solidification conditions while also reducing the computational resources needed.

2. Theory

2.1 Problem Statement

The problem of determining what scan path gives the desired site-specific microstructure has an effectively infinite search space. In E-PBF, the heat source can effectively change locations instantaneously which means for every decision when constructing a scan path, every point on the geometry must be considered. The instructions at these points usually consist of either spot melts or line melts. Spot melts are described by the point the heat source is centered on and how long the heat source remains on that point, called the spot time. Line melts are described by the point at which the heat source is initially centered on, the point where the line melt ends, and the speed on the heat source. Much like previous attempts [8,33], the problem is made tractable by restricting the considered points to a constant, regular grid while also having the scan path solely consist of spot melts.

Despite these simplifications, the problem still possesses an immense search space. Previous attempts required a plethora of simulations which is why analytic models, known for being computationally inexpensive, were used. These attempts also simulated only the **solidification conditions of the top surface** to further reduce the computational expense, though such an approach may be seen as unphysical since the **resulting microstructural estimation** (via the solidification conditions) on the top surface may not relate well to the bulk microstructure. **Estimating the bulk microstructure via simulating the entire 3D temperature field** is undoubtedly a more physical approach; however, calculating the temperature field throughout the depth of a part increases the computational expense by at least an order of magnitude over surface-only calculations.

This paper seeks to use an alternate approach, which revolves around the use of a surrogate model to circumvent the expensive 3D **thermal** simulations required to calculate the bulk solidification conditions **resulting from a spot melt**. The proposed general method consists of three components (Figure 1):

1. A heat transfer model for simulating the temperature field at a given time.
2. A surrogate model which **takes scan pattern information and temperature data** and predicts the solidification conditions of the bulk as well as the meltpool depths for a spot melt.
3. A decision algorithm to decide which spot melt should be printed next based on the outputs of the surrogate model.

The main advantage of this approach is being able to quickly predict the results **of a set of spot melts via repeated use of the surrogate model**. In this way, the decision algorithm can be given a set of **many potential spot melts to consider adding to the scan path**. By circumventing the heat transfer simulations needed to calculate the 3D results a spot melt, most of the computational cost of this

method is front-loaded onto the creation of the surrogate model which consists of three components itself (Figure 1):

1. A generator algorithm for creating a robust set of heat transfer conditions **via scan pattern generation**.
2. A heat transfer model for simulating the solidification conditions of the bulk as well as the meltpool depth **for a spot melt which immediately follows the scan pattern given by the generator algorithm**.
3. A surrogate model which **takes scan pattern information and temperature data** and predicts the solidification conditions of the bulk as well as the meltpool depths for a spot melt.

Ensuring this surrogate model is robust is paramount to the success of this method. **A robust surrogate model is one in which performs well when encountering new or noisy data. In machine learning, robustness is observed from either having the testing set perform similarly to the training set or by having stable performance after adding some noise. To ensure robustness, the dataset fed used in the creation of a surrogate model should be representative of what can be encountered. The purpose of the generator algorithm is to create this representative dataset which, in this work, consists of scan path information.**

It should be noted that the more expensive heat transfer simulations involved in calculating bulk solidification conditions and meltpool depths only need to be run while training the surrogate model. In the application of this method, the heat transfer simulations are only used in generating the temperature field.

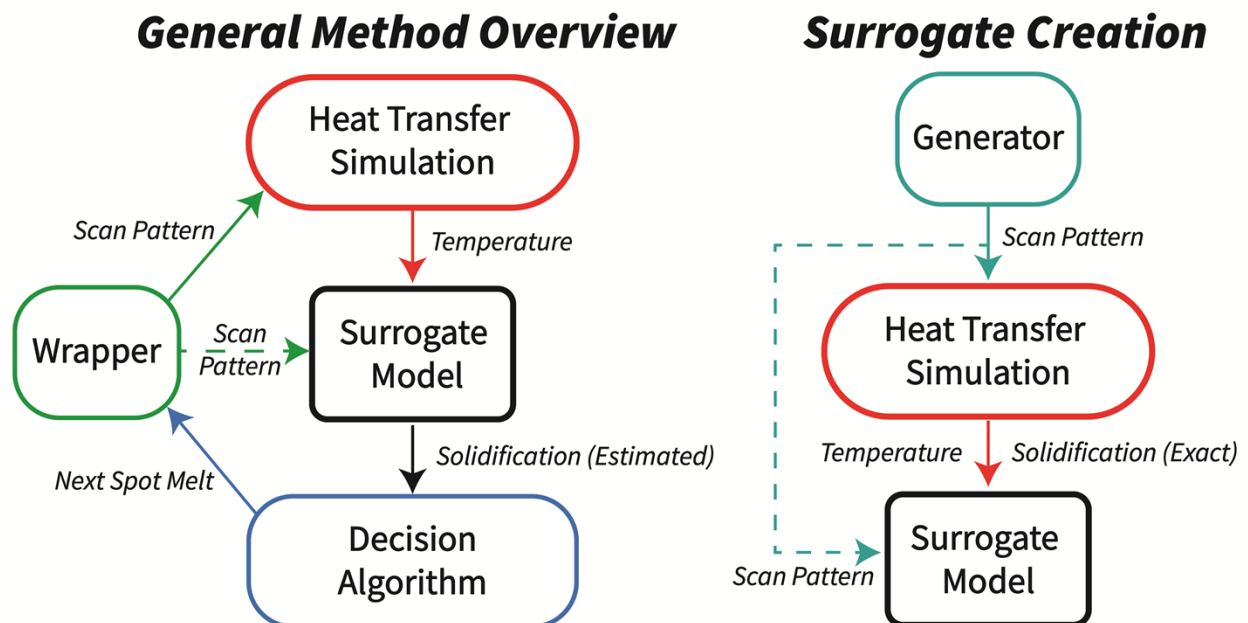


Figure 1: Two flowcharts detailing the general optimization method (left) and creation of a surrogate model (right). In the general optimization method (left), the heat transfer simulation is only used to generate the temperature

field; however, when creating the surrogate model (right), the heat transfer simulation also calculates the solidification conditions.

2.2 Microstructure Model

Relating solidification conditions to microstructural properties is a complicated problem in and of itself; however, the problem can be simplified by using the approximate model (eq. 1) derived by Gaumann [19] for the columnar to equiaxed transition (CET). Gaumann's CET model extends the original work by Hunt [35] to non-equilibrium conditions similar to those in additive manufacturing. The CET model itself considers two types of grain morphologies: equiaxed and columnar. Equiaxed grains tend to have random crystallographic orientations whereas columnar grains tend to have strong crystallographic orientations relating to the thermal gradient. These broad grain morphologies are of interest because, on a macroscopic scale, equiaxed grains have nearly isotropic properties whereas columnar grains have anisotropic properties.

The output of the CET model (Eq_{frac}) describes the volumetric fraction of grains which are equiaxed rather than columnar in space (Eq_{frac}) from information about the thermal history (solidification gradient (G) and solidification velocity (V)) and material information (density of nucleation sites (N_0) and material dependent constants (n , a) which relate the undercooling of the dendrite tips to the solidification velocity (V) given in equation 2). The values of $a = 1.25 \times 10^6$, $n = 3$, and $N_0 = 3 \times 10^{13}$ have previously been used for Ni-base superalloys and although these exact values are not critical for the present work, calibration of these values is necessary for actual application [20]. It should be noted that these values do allow for a range of Eq_{frac} given the processing parameters found in additive manufacturing applications [10,36]. For other materials which do not give a range of Eq_{frac} for typical processing parameters, this work cannot be expected to give control over grain morphology.

$$Eq_{frac} = 1 - \exp \left[-\frac{4}{3} \pi N_0 \left(\frac{(aV)^{1/n}}{G(1+n)} \right)^3 \right] \quad (1)$$

$$\Delta T_c = (aV)^{1/n} \quad (2)$$

2.3 Repeated Element

The concept of the repeated element was devised to better predict the bulk microstructure from the solidification conditions predicted via simulation. In the literature, there have been several instances where thermal simulations consist of either a single layer or just the top surface [10,34]. This approach neglects the re-melting of material and can lead to a disconnect between modeling results and the actual microstructure. The solidification conditions for just the top surface, or even an entire single layer, are not representative of the bulk microstructure because much of this material is remelted on subsequent layers.

If the interlayer preheat is identical, the solidification conditions of each layer with the same processing parameters and scan path area also identical. Using these assumptions for two consecutive layers, the portion of material which is not remelted on the first layer is directly related to the layer thickness (Δz) of a build. If these same assumptions are applied to an entire build, only the bottom Δz of

each layer will remain. It should be noted that a consequence of having only the bottom Δz of a layer remain is not all meltpools will directly impact the final solidification conditions of the bottom Δz . Instead, some of these meltpools may indirectly affect the final solidification conditions through their deposited energy affecting the thermal field and thus the solidification conditions resulting from future meltpools. In this way, melting events can be split into two categories: *printable melts*, which directly influence the final solidification conditions of the bottom Δz , and *heatable melts*, which do not.

The idea of the repeated element is encapsulated in Figure 2 which is constructed using a series of repeated spot melts. Figure 2a depicts the equiaxed fraction for the entire layer whereas Figure 2b depicts the stacked result of 4 identical layers, using $\Delta z = 50\mu\text{m}$, with a repeated element outlined in yellow. In the single layer case (Figure 2a), there seems to be solidification conditions that would lead to a mixture of equiaxed and columnar microstructures; however, once the layers are stacked upon each other (Figure 2b), it becomes apparent that only the columnar, or $Eq_{frac} \sim 0$, grain morphology would persist throughout a build. Throughout the rest of the paper, Eq_{frac} refers average grain morphology of the repeated element which was created through this method of shifting.

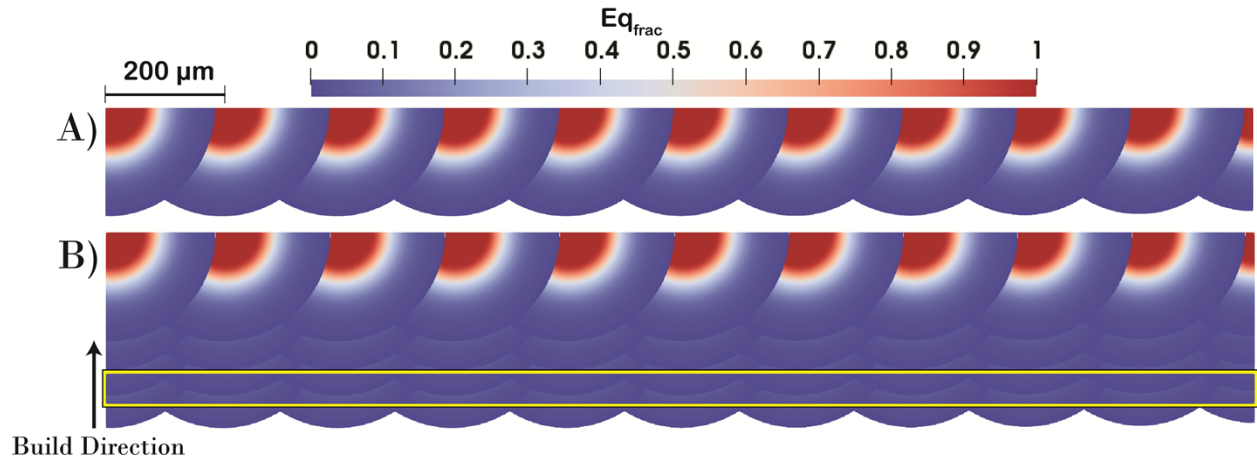


Figure 2: Showing the equiaxed fraction for the center cross section of repeated spot melts for a single layer (A) and multiple, repeated layers (B). The repeated element is highlighted in yellow.

3. Methods

3.1 Heat Transfer Model

The heat transfer model chosen is based on the semi-analytic solution to an arbitrarily moving volumetric Gaussian heat source within a semi-infinite domain (eq. 3) [37] where T_0 represents the initial temperature, Q the beam power, η the absorption efficiency, and α the thermal diffusivity of the material. The volumetric heat source is described by widths σ_x , σ_y , and σ_z . The coordinates $\vec{x} = \langle x | y | z \rangle$ are the relative distances between the point of interest \vec{x}_p and the transient position of the beam $\vec{x}_b(t')$. Though there exist several programmatic implementations of this equation, the implementation containing an adaptive integration scheme [27] was chosen due to its speed, ease of use, and other beneficial features, such as *Meltpool Tracking* which can greatly decrease computational expense by only requiring calculations for liquid points. The solidification conditions can also be calculated using equations 4a, 4b, and 4c.

$$\Delta T(t) = \frac{2\eta Q}{\rho c(\pi/3)^{3/2}} \int_0^t \frac{1}{\sqrt{\phi_x \phi_y \phi_z}} \exp\left(\frac{-3x(t')^2}{\phi_x} - \frac{3y(t')^2}{\phi_y} - \frac{3z(t')^2}{\phi_z}\right) dt', \quad (3)$$

where $\phi_i = 12\alpha(t - t') + \sigma_i^2$ for $i = x, y, z$.

$$\vec{G} = \frac{d\Delta T(s)}{d\vec{x}} \quad (4a)$$

$$\dot{T} = \frac{d\Delta T(s)}{dt} \quad (4b)$$

$$V = \frac{\dot{T}}{|G|} \quad (4c)$$

The purpose of the heat transfer model is to take a scan path and generate the outputs of interest. These outputs of the heat transfer model depend on how the model is being used. When the heat transfer model is used to generate training data, the relevant inputs to the surrogate model (surface temperature T) and relevant outputs of the surrogate model (grain morphology of the repeated element Eq_{frac} and maximum depth of the resulting melt pool d) must be calculated. When the heat transfer model is used in the application, only the input into the surrogate model (surface temperature T) must be calculated. All heat transfer simulations in this work use the properties found in Table 1.

Table 1: Simulation Properties

Properties	IN718	Units
Material:		
Density, ρ	7451	kg/m ³
Specific heat capacity, c_p	600	J/(kg K)
Thermal conductivity, k	26.6	J/(m s K)
Preheat Temperature, T_0	1273	K
Liquidus Temperature, T_{liq}	1610	K
Other:		
Grid Spacing, Δx	200	μm
Layer Thickness, Δz	50	μm
Base Spot Time, Δt_0	50	μs
Beam:		
Beam Power, P	1200	W
Absorption Efficiency, η	0.80	
Beam Diameter, $\sigma_{x,y}$	300	μm
Penetration Depth, σ_z	10	μm

3.2 Generator Algorithm

To create a robust surrogate model, the dataset used should contain a wide range of conditions akin to what may be encountered during application. The generator algorithm is designed to create entire, random scan paths which should give complex, transient temperature profiles. Such randomness is expected to satisfy the requirements for a robust set of inputs to the surrogate model; however, it is important to ensure that these inputs also result in a robust set of outputs $\{Eq_{frac}, d\}$.

To make the results more physical, the application itself was tailored towards being able to run on an E-PBF system. Spot times in E-PBF systems are quantized; therefore, an integer spot time multiplier $M_{i,j}$ is used along with the base spot time Δt_0 to control the spot time in a physically applicable way (eq. 5). Much like in Halsey's method [34] for microstructure control, these are set to $\Delta t_0 = 50\mu s$ and $M_{i,j} \in \{1,2,3,4,5\}$. Furthermore, to differentiate between the previously chosen spot time multipliers and spot time multiplier for the next spot melt, $M_{i,j}$ and $M_{i,j}^*$ are used respectively.

$$\Delta t_{i,j} = M_{i,j} \Delta t_0 \quad (5)$$

If the set of inputs only includes the surface temperature at the point $T_{i,j}$ and the next spot time multiplier $M_{i,j}^*$, then the transient nature of the temperature field is neglected; however, information about the scan path, which indirectly gives data about the diffusion of the temperature field, can be used instead to inform the surrogate model of this transience. To encode information about the transient nature of the temperature field, a new variable Φ (eq. 7) is introduced which serves as the nondimensional replacement to ϕ from the semi-analytic solution (eq. 3). The formulation for the nondimensional form of the semi-analytic solution is given in [27]. Φ serves the purpose of letting the surrogate network know how long a previous spot has been able to diffuse in nondimensional time s . Using Φ alongside $M_{i,j}$, which gives knowledge of the previous amounts of energy deposited at each point given, the transient nature of the temperature field at \vec{x}_p can be approximated.

$$\Phi_{i,j} = (12s + 1)^{-1/2}, \text{ where } s = \frac{\alpha(t - t_{i,j})}{\sigma_{x,y}^2} \quad (7)$$

The reason for choosing to roughly approximate the transient nature of the temperature field at \vec{x}_p using scan pattern information at rather than from more precise calculation through considering the temperature field (either 2D or 3D) near \vec{x}_p is due to the greatly reduced computational workload. Being able to generate data of just a single surface point alongside the points directly below it, via *Meltpool Tracking*, takes advantage of the unique capabilities of the analytic model.

This single surface point, referenced as $p_{0,0}$, lies in the center of a large, rectangular grid. This grid is set to have 251 points in the x and y directions; therefore, the values of the grid point indices $\{i,j\}$ lie in the range $[-125,125]$. By only simulating $p_{0,0}$ and the points below it rather than all $p_{i,j}$ potentially reduces the computational load of generating a datapoint for the surrogate model by over 10,000x. Since some surrogate models, such as the neural network used in this paper, function much

better with large datasets, this speedup allows for an appreciably large dataset to be produced on a desktop computer rather than a supercomputing cluster.

The specific way the generator algorithm creates the dataset is by creating random scan paths on this grid to give a complex temperature profile before a spot melt is printed at $p_{0,0}$ with a random $M_{0,0}^*$. The algorithm records the inputs before the final spot melt. These inputs are the scalar values $T_{0,0}$ and $M_{0,0}^*$ as well as the scan pattern information of the grid given by $\Phi_{i,j}$ and $M_{i,j}$ for all $\{i,j\}$. The resulting outputs are recorded at $p_{0,0}$ after this final spot melt has solidified and consist of Eq_{frac} and d normalized to the range (0,1).

The random scan patterns are each given a global variable called the random point print probability $P \in [0.02,0.50]$ which dictates the likelihood individual points are printed. The generator algorithm considers each point $p_{i,j}$, including $\{i,j\} = \{0,0\}$, in a random order and decides, based on P , if the point should be printed. If it is printed, $p_{i,j}$ is given a random $M_{i,j}$. Higher values for P typically result in warmer temperature fields whereas lower values for P result in cooler temperature fields. This method of random scan pattern generation resulted in a wide range of values for d but lacked many potential values for Eq_{frac} (Figure 3).

To remedy this problem, two additional concepts are introduced to help lower the thermal gradients around $p_{0,0}$ before the final spot melt. The first concept is to cluster the points at the end of a scan pattern to be around $p_{0,0}$. To do this, each scan pattern was assigned an additional global variable called the Gaussian weight $\omega \in [-2,10]$. This is used in conjunction with a measure of distance between $p_{i,j}$ and $p_{0,0}$, to create a metric (Θ_{mult}) which is used to change the order in which the points are considered (eq. 6). When creating a random scan path, the order is decided by giving each point a unique integer number $\Theta \in [1,251^2]$ and sorting in ascending order based on Θ . Θ_{mult} is used in the creation of a new number $\Psi = \Theta * \Theta_{mult}$ before resorting based on the newly calculated value of $\Psi \in (0,251^2]$. The result of this is that larger values of ω results in the spots melts towards the end of the scan path being more clustered around $p_{0,0}$.

$$\Theta_{mult} = e^{-\omega \left(\frac{i^2+j^2}{125^2} \right)} \quad (6)$$

The second concept introduced is allowing a random number of scan patterns (between 2 and 10) to be concatenated together thus allowing for the heat to both buildup and diffuse before the final spot melt. To account for the increase in total deposited heat from multiple scan patterns, the maximum value for the random point print probability P was lowered from 0.50→0.25. The results of this revised generator algorithm gave a good mixture of the desired inputs (Figure 3). The datasets from the two iterations, each with over 10^4 unique samples, were combined into the larger dataset which the surrogate model was trained on.

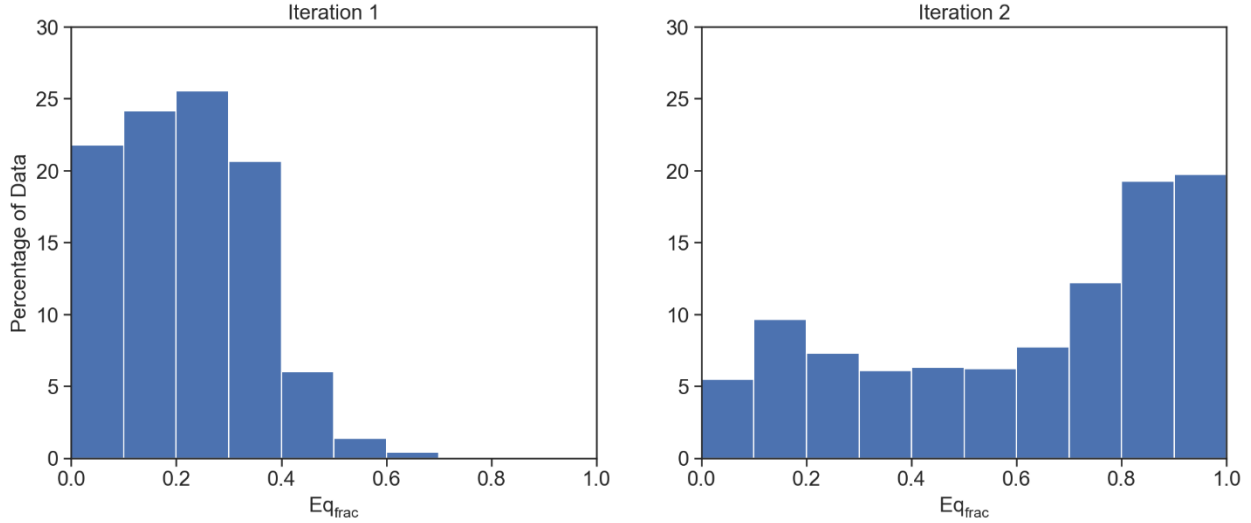


Figure 3: Histogram showing the different iterations of the data synthesis algorithm and the resulting equated fractions

3.3 Surrogate Model

The job of a surrogate model is to accurately predict a set of outputs given a set of inputs. Since the mapping of $\{T, M^*, M, \Phi\} \rightarrow \{Eq_{frac}, d_{pred}\}$ is likely highly nonlinear, neural networks, which are routinely used for such a task, are the approach of choice. The specific neural network architecture used here is called a Fully Convolutional Neural Network (FCNN) which is designed to keep the spatial dimensionality of the inputs and outputs the same. Additionally, physical intuition says this FCNN should be rotationally invariant since viewing the same scan from different orientations should yield the same results at each point on a part.

Rather than constrain the FCNN to be rotationally invariant, the dataset was augmented to contain this same invariance which has been shown to produce similar results [38] while also being easier to implement. The full structure of the FCNN is given in Figure 4 with the total number of inputs shown in Table 3. The design of the FCNN follows as such:

- *Input 1* consists of the of the local information about a point pertaining to the transient nature of the thermal field: $M_{i,j}$ and $\Phi_{i,j}$.
- The *Diffusion Module* gradually widens the network, using a sequence of 1x1 convolutions, allowing the necessary parameters for understanding the transient nature of the previous spot melts to be learned.
- The *Locality Module* then uses increasingly large convolutions to give $p_{0,0}$ information the necessary information about transient nature of the nearby temperature field. These convolutions are restricted to be odd and square (1x1, 3x3, 5x5...) to ensure $p_{0,0}$ is always at the center of each convolutional filter.
- *Input 2* consists of $T_{0,0}$ and $M_{0,0}^*$ and is concatenated with the output of the *Locality Module*.

- The *Solidify Module* then narrows the network, using a sequence of 1x1 convolutions, until there are two outputs, one for both Eq_{frac} and d , at $p_{0,0}$. The purpose of these repeated 1x1 convolutions is to increase the depth of the network [39] to better capture complex nonlinearities.

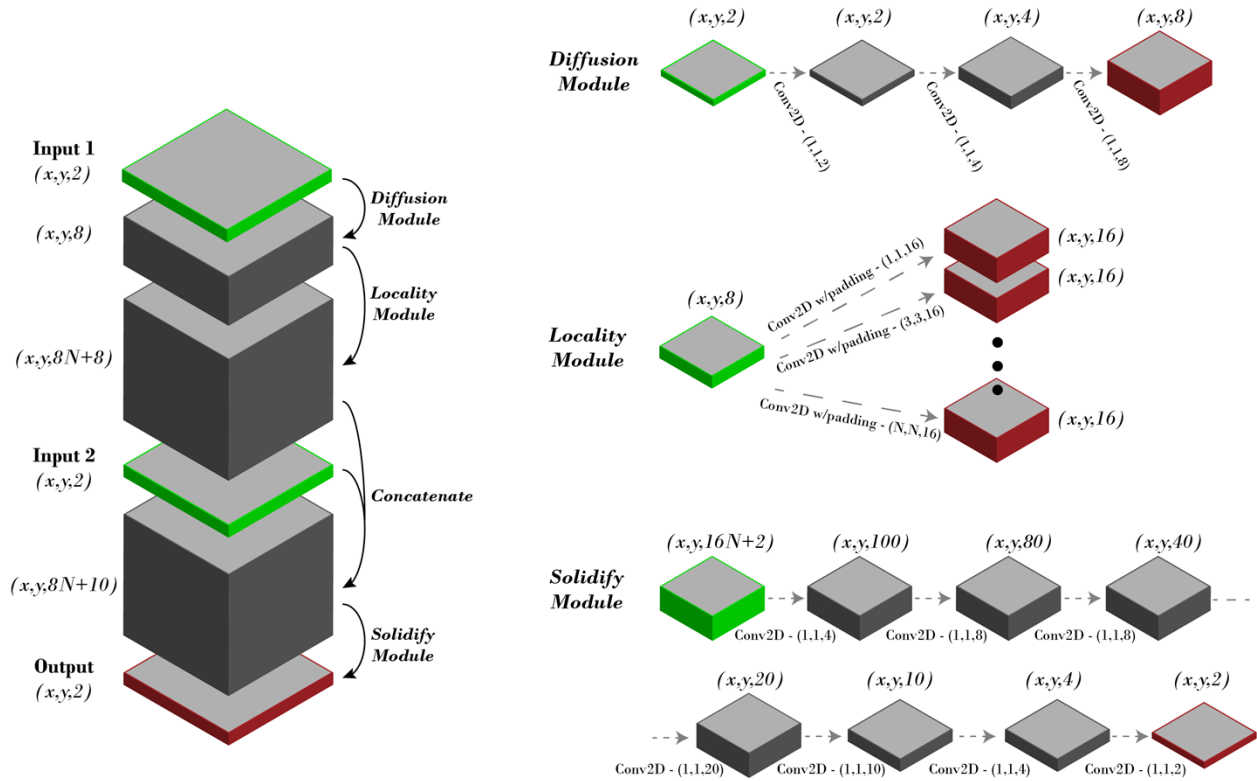


Figure 4: Diagram of the Fully Convolutional Neural Network.

The training of the FCNN was done in Python using the TensorFlow packing via the AdaMax [40] optimizer with the default hyperparameters ($lr = 0.002, \beta_1 = 0.9, \beta_2 = 0.999$) and using the mean absolute percentage error loss function [41]. The Leaky ReLU ($\alpha = 0.1$) activation function is used for each of all but the last layer to help avoid the problem with vanishing/exploding gradients in deep FCNNs as well as provide superior performance over the conventional ReLU activation function [42]. The final activation function is a sigmoid which puts both outputs in the range (0,1). The validation split, fraction of batch size to training set size, and number of epochs per batch are listen in Table 2. Finally, rather than decrease the learning rate over time, the batch size was increased which has been shown to have a similar effect [43].

Table 2: Training Parameters for the Neural Network

Properties	Value
Optimizer	AdaMAX
Activation Function	Leaky ReLU
Loss Function	Mean Absolute Percentage Error
Validation Split	5%
Batch Size Fractions	[64, 128, 256, 512, 1024, 2048, 4096, 8192]
Epochs	[100, 100, 100, 100, 100, 100, 100, 100]

The question which arises here is how large should the maximum convolutional filter in the *Locality Module* be? Since the size of the convolutional filters in the *Locality Module* can become arbitrarily large (up to 251x251), a convergence study was done to find a cutoff size where performance does not significantly increase based on the final training and test losses (Table 3). All maximum filter sizes resulted in robust surrogate models (since the test loss is similar to the training loss) but using a large maximum filter size vastly improved the accuracy of the surrogate model. The maximum filter size was chosen to be 11x11 since performance did not significantly increase from the 9x9 maximum filter size.

Table 3: Architecture Study for Various Maximum Convolutional Sizes in the Locality Module, denoted by N.

N	Number of Trainable Parameters	Training Loss	Test Loss
1	14,506	32.8	35.1
3	17,274	18.2	18.5
5	22,090	9.8	10.2
7	29,978	6.4	6.7
9	41,962	3.7	4.3
11	59,066	3.1	3.9

The resulting surrogate model, due to the architecture chosen, can be trained on the dataset given by the generator algorithm, which has inputs T and M^* just residing at $p_{0,0}$, but applied on many points simultaneously so long as the grid layout is identical to what was used when training. This is ideal since, during an application, the surrogate model computes the outputs $\{Eq_{frac}, d\}$ at every $p_{i,j}$ with little computational expense. Additionally, every $M_{i,j}^* \in \{1,2,3,4,5\}$ can also be considered by running the surrogate model once per value. In essence, the surrogate model, during application, quickly gives the predicted outputs for every $\{p_{i,j}, M_{i,j}^*\}$ pair. The question is, given all these predictions, how should the next spot melt be chosen?

3.4 Decision Algorithm

The purpose of the decision algorithm is to select what action to do next given the output from the surrogate model. Since the surrogate model gives many outputs due to calculating $\{Eq_{frac}, d\}$ at every $\{p_{i,j}, M_{i,j}^*\}$ pair, a greedy algorithm was used due to its simplicity. A greedy algorithm is one in which only the action with the highest immediate reward is chosen. Though this neglects future planning, greedy algorithms achieve good results for many applications. The reward fed into the greedy algorithm is defined as the inverse of the binary cross entropy H_b (eq. 8) between the predicted equiaxed fraction y and desired equiaxed fraction \hat{y} . H_b is a measure of how closely the predicted repeated element of that point matches what is desired and is routinely used in classification problems where the desired values are either 0 or 1 but the computed values lie in the range (0,1). A low H_b means the two values are similar whereas a high H_b indicates the opposite.

$$H_b = -\hat{y} \log y - (1 - \hat{y}) \log(1 - y) \quad (8)$$

The predicted value of d (d_{pred}) is used to further narrow the choices since requiring the final value of d (d_{melt}) to be reasonably uniform across a part prevents a spot melt at some point from interfering with the repeated element of its neighboring points. Based on d_{pred} , the possible actions can be narrowed into two categories: printable and heatable. A printable action is a spot melt at a point where the resulting predicted depth is close to the desired final depth ($|d_{melt} - d_{pred}| < \Delta z$) and another printable action at that point has not yet been done. A heatable action is a spot melt at a point which is not expected to interfere with the expected final repeated element of the point ($2d_{pred} < d_{melt}$). Any number of heatable actions can occur at a point while only one printable action can ever be done at a point. Once printable actions have been taken at all points, the scan pattern generation is complete.

Separating actions into these two categories and having a defined reward is not enough to ensure the decision algorithm makes good choices. For instance, imagine a scenario where many points have already been printed. The reward for actions at these points does not matter since any actions must be heatable actions which will not change the equiaxed fraction of the repeated element. Additionally, for the unprinted points, if all remaining actions result in poor rewards, should these points be printed or heated? To remedy this, a decision structure is designed based on the general understanding of what conditions may lead to a spot melt resulting in either an equiaxed or columnar repeated element (Figure 5). Generally, spot melts leading to equiaxed repeated elements require more preheating than for spot melts leading to columnar repeated elements and should thus be generally printed later. Consequentially, this means they should also be heated first.

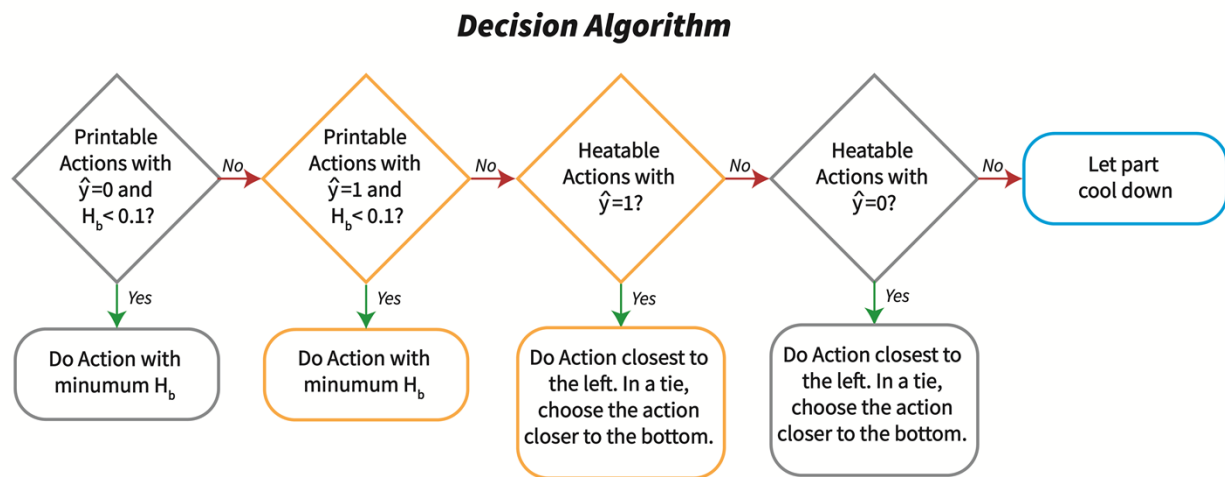


Figure 5: Diagram showing the order spot melts are considered by the Neural Network. Silver denotes points with a desired columnar grain morphology whereas gold denotes a desired equiaxed grain morphology.

The first step in this decision structure is to see if there exists a printable action for points with desired $Eq_{frac} = 0$. If there exists printable action with an H_b less than a certain allowable value ($H_{b,max} = 0.1$), then the printable action with the minimum H_b is taken. If an action does not exist, then printable actions for points with desired $Eq_{frac} = 1$ are considered in the same manner. If there exist no printable actions, then the system must either heat or cool. When choosing to heat the part, points with desired $Eq_{frac} = 1$ are considered first. The point closest to the bottom left which has not undergone a

printable action is chosen. From here, a random nearby (within 11x11) heatable action is done. If there exists no such heatable action, the next unprinted point with $Eq_{frac} = 1$ is chosen and the process repeats. If no heatable action can be done for any remaining point with $Eq_{frac} = 1$, the same process is done with the points with desired $Eq_{frac} = 0$. Finally, if no printable or heatable actions can be taken, the system cools for $\Delta t_{cool} = 5\Delta t_0$.

4. Results and Discussion

The use of this application requires two inputs: a binary image which dictates the desired Eq_{frac} at a given point as well as a value for d_{melt} . To demonstrate the utility of this approach as well as pay homage to the supporting organization, a binary image of the MDF logo, with the letters “MDF” being given a value of 1, was given to the algorithm alongside a value of $d_{melt} = 400\mu m$. The dimensions of the image, when converted using the $200\mu m$ grid spacing, is 52x28mm. The total runtime of this program was roughly 10 hours on a single desktop using 4 cores of an Intel Core i7-7820X CPU operating at 3.60GHz. The input image alongside the resulting Eq_{frac} are given in Figure 6. It should be noted that the results shown in Figure 6 are taken from a full 3D simulation using the analytic model and not from what the surrogate model predicted before each spot melt during the application.

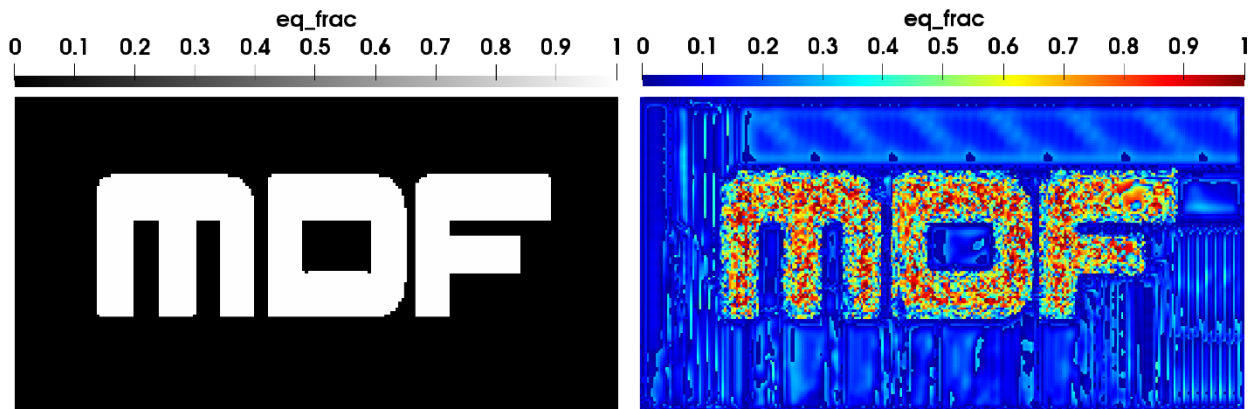


Figure 6: The NN input image (left) and the bottom surface of the analytic simulation (right) using the scan path generated by the NN.

The first thing to notice is how clear the letters “MDF” can be seen in the image showcasing the resulting Eq_{frac} . Other than the bottom left corner of the letter “D,” the application achieved fine control of the simulated grain morphologies. The second thing to notice is how much better the application performed in the regions with desired columnar grains. Although the “MDF” is clearly distinct from the background, many values within the “MDF” are far from their target value of 1. To determine why this might be the case, the scan path was visualized. The partial visualization of the scan path is shown in Figure 7 by simulating the surface temperature at various points in time with a sharp transition in the colormap occurring at the liquidus temperature.

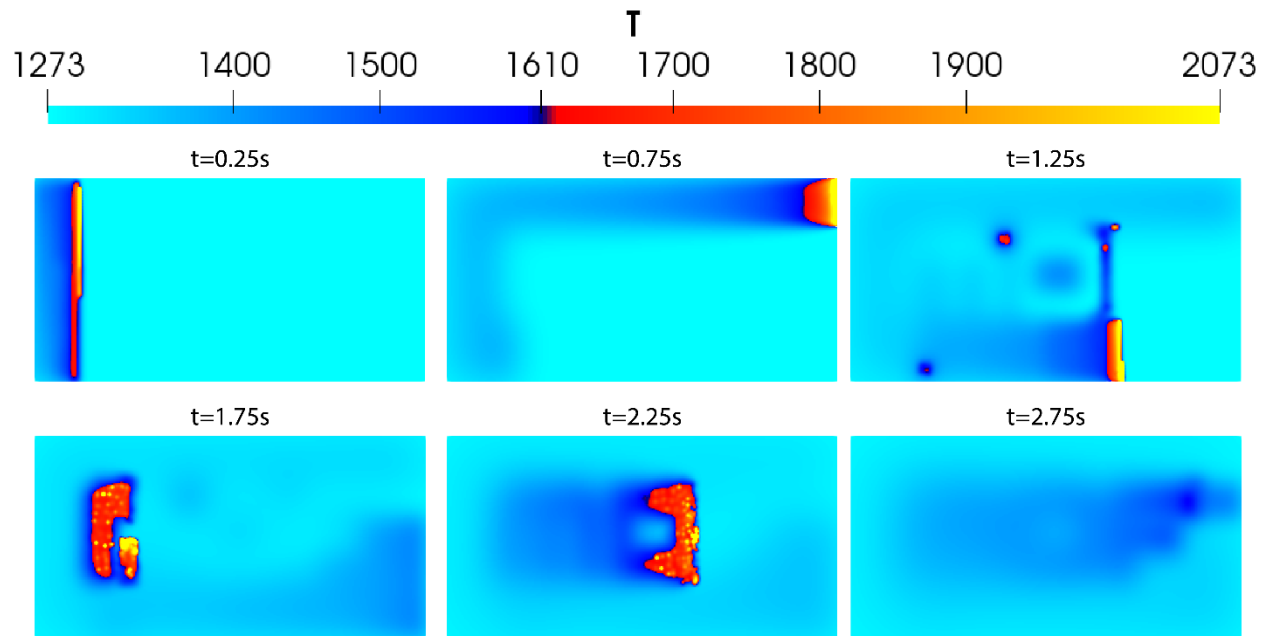


Figure 7: The temperature profile of the top surface of the simulated domain at 6 different times

The resulting algorithm prefers to generate pseudo-raster patterns in sections where the desired grain morphology is columnar; whereas, in sections where the desired grain morphology is equiaxed, the resulting algorithm prefers to generate area melts. This result is both surprising and encouraging since, in the field of additive manufacturing, raster patterns have been historically used to generate columnar grains whereas area melts have recently been gaining traction for generating equiaxed grains [9,36,44]. It seems that although the surrogate model was trained on a large amount of spot melt patterns, the resulting algorithm still learns to generate approximate raster patterns through repeated adjacent spot melts.

From these types of scan patterns, the difference in error between the resulting Eq_{frac} in the desired columnar and desired equiaxed sections can be explained. The basis of this algorithm is the use of a surrogate model which predicts the solidification conditions of the bulk as well as the meltpool depths for a spot melt by considering the scan pattern information and temperature data. During dataset generation, this data is collected from the final spotmelt of a scan pattern. Keep in mind that this is necessary as encoding information about future spotmelts is nonsensical since in the actual application, which is an optimization algorithm, these cannot be known.

This method means that these predictions will become less accurate the more future spot melts interfere with the thermal conditions during solidification. For the pseudo-raster sections, where the distance of future spot melts from a given spot melt's solidification increases, the outputs of the surrogate model are more accurate. On the other hand, for the area melts, where many nearby spot melts may occur during a given spot melt's solidification, the outputs of the surrogate model will be less accurate. With this in mind, the application may seem to do surprisingly well but it should be emphasized that many of the nearby spot melts in the area melt section come from heatable actions which are typically shorter in duration and designed to result in shallow meltpools. Lastly, these equiaxed sections need to be at least 1mm from the edges of the part (preferably 1mm). Since this

algorithm decides to do area melting around equiaxed sections, having an equiaxed section close to the edge can give underwhelming results.

5. Conclusions and Future Work

Being able to generate scan paths based on location specific desired microstructure would be able to significantly improve part performance. Currently, only E-PBF systems can achieve this due to the near instantaneous movement of the heat source. Procedurally generating such scan paths has only recently been considered due to advances in computational applications. This paper introduces a general scan path optimization method which has been shown to quickly create robust scan patterns intending to control the microstructure.

The general scan path optimization method contains three essential components and is applied two different times using varying levels of complexity for all three components:

1. A heat transfer model for simulating the temperature field at a given time.
2. A surrogate model which **takes scan pattern information and temperature data** and predicts the solidification conditions of the bulk as well as the meltpool depths for a spot melt.
3. A decision algorithm to decide which spot melt should be printed next based on the outputs of the surrogate model.

The application used in this work consists of a analytic heat transfer model, an FCNN as the surrogate model, and a greedy decision algorithm. The semi-analytic heat transfer model allowed for quick generation of a massive dataset which the FCNN was trained on. The greedy decision algorithm was designed around physical intuition about the thermal conditions which may lead a spot melt to give either a columnar or equiaxed grain morphologies. This algorithm was then run on a sample binary microstructure where the letters “MDF” were desired to consist of equiaxed grains. The resulting simulated microstructure aligned closely with what was desired provide a look into the future of microstructure control when utilizing the full capabilities of E-PBF systems.

There are many directions to this work next. The most obvious direction is to print the actual part on an E-PBF machine. The results of such an experiment would not be expected to completely coincide with the simulated microstructure but rather help guide further research. For instance, maybe a “MDF” is printed which can clearly be seen but is messy and lacks the fine microstructure control shown in Figure 7. The areas in which the algorithm fails or succeeds should give insights into the shortcomings of the algorithm. These expected shortcomings may be a result of the nature of the analytic model or the choice of parameters for the CET model which further work could help narrow down.

Additionally, the computational framework is far from optimal. Not only does every iteration require a complete rerun of the analytic model (including lots of file I/O) but none of it is being accelerated via GPUs. If the entire optimization algorithm was combined into one code and ported to GPU, a speedup of 50x or more could be expected. This would allow a single desktop computer to optimize the simulated microstructure of a single layer in just minutes. Given even a moderate compute cluster, optimizing the simulated microstructure of an entire build would be possible.

The analytic model itself could also be replaced with a higher-fidelity heat transfer model. It has been shown in higher-fidelity models that physics which are local to the melt pool do not have a large impact on the solidification conditions [45]; however, the lack of larger-scale physics pertaining to heat transfer, such as non-linear heat conduction, may make a notable difference on the long length and time scales of the generated scan paths. For example, raster patterns, where the thermal conditions surrounding the heat source are relatively similar throughout a build, can have the constant thermal diffusivity calibrated effectively. For more complex scan patterns, such as the ones used in the simulations presented in this paper calibrating to a constant thermal diffusivity is nonsensical since each revisit to an area will have different temperature fields. Using the analytic model, these temperature fields will depend heavily on the value chosen for the thermal diffusivity which may lead to the calculated values being substantially different than those of a higher-fidelity model.

Finally, replacing the greedy algorithm with a reinforcement learning (RL) approach would be ideal. An algorithm which uses reinforcement learning would be able to consider its future actions thus eliminating the shortcoming of the current work where the surrogate model cannot consider future spot melts. Additionally, such an approach would remove the human priors used to generate the decision algorithm in this work which may give rise to solutions stemming from superior heuristics.

Acknowledgements

This research was performed at the Department of Energy's Manufacturing Demonstration Facility located at Oak Ridge National Laboratory.

This manuscript has been authored by UT-Battelle, LLC under Contract No. DE-AC05-00OR22725 with the U.S. Department of Energy. Research was co-sponsored by the U.S. Department of Energy, Office of Energy Efficiency and Renewable Energy, Advanced Manufacturing Office and the Office of Electricity Delivery and Energy Reliability (OE) – Transformer Resilience and Advanced Components (TRAC) Program. The United States Government retains and the publisher, by accepting the article for publication, acknowledges that the United States Government retains a non-exclusive, paid-up, irrevocable, world-wide license to publish or reproduce the published form of this manuscript, or allow others to do so, for United States Government purposes. The Department of Energy will provide public access to these results of federally sponsored research in accordance with the DOE Public Access Plan (<http://energy.gov/downloads/doe-public-access-plan>).

The author would like to thank Alex Plotkowski and Gerald Knapp and for reviewing this work and providing valuable feedback.

Data Availability

The raw/processed data required to reproduce these findings cannot be shared at this time due to technical or time limitations.

References

- [1] T. DebRoy, H.L. Wei, J.S. Zuback, T. Mukherjee, J.W. Elmer, J.O. Milewski, A.M. Beese, A. Wilson-Heid, A. De, W. Zhang, Additive manufacturing of metallic components – Process, structure and properties, *Prog. Mater. Sci.* 92 (2018) 112–224. doi:10.1016/j.pmatsci.2017.10.001.
- [2] Y. Kok, X. Tan, P. Wang, M.L. Nai, N. Loh, E. Liu, S. Tor, Anisotropy and heterogeneity of microstructure and mechanical properties in metal additive manufacturing: A critical review, *Mater. Des.* 139 (2018) 565–586.
- [3] W.J. Sames, F.A. List, S. Pannala, R.R. Dehoff, S.S. Babu, The metallurgy and processing science of

- metal additive manufacturing, *Int. Mater. Rev.* 61 (2016) 315–360.
doi:10.1080/09506608.2015.1116649.
- [4] J. Raplee, A. Plotkowski, M.M. Kirka, R. Dinwiddie, A. Okello, R.R. Dehoff, S.S. Babu, Thermographic Microstructure Monitoring in Electron Beam Additive Manufacturing, *Sci. Rep.* 7 (2017) 1–16. doi:10.1038/srep43554.
- [5] A. Plotkowski, J. Pries, F. List, P. Nandwana, B. Stump, K. Carver, R.R. Dehoff, Influence of Scan Pattern and Geometry on the Microstructure and Soft-Magnetic Performance of Additively Manufactured Fe-Si, *Addit. Manuf.* 29 (2019) 100781.
- [6] G.P. Dinda, A.K. Dasgupta, J. Mazumder, Texture control during laser deposition of nickel-based superalloy, *Scr. Mater.* 67 (2012) 503–506. doi:10.1016/j.scriptamat.2012.06.014.
- [7] N. Raghavan, S. Simunovic, R.R. Dehoff, A. Plotkowski, J. Turner, M.M. Kirka, S.S. Babu, Localized Melt-Scan Strategy for Site Specific Control of Grain Size and Primary Dendrite Arm Spacing in Electron Beam Additive Manufacturing Localized Melt-Scan Strategy for Site Specific Control of Grain Size and Primary Dendrite Arm Spacing in Electron, *Acta Mater.* 140 (2017) 375–387. doi:10.1016/j.actamat.2017.08.038.
- [8] R.R. Dehoff, M.M. Kirka, W.J. Sames, H. Bilheux, A.S. Tremsin, L.E. Lowe, S.S. Babu, Site specific control of crystallographic grain orientation through electron beam additive manufacturing, *Mater. Sci. Technol.* 31 (2015) 931–938. doi:10.1179/1743284714Y.0000000734.
- [9] M.M. Kirka, Y. Lee, D.A. Greeley, A. Okello, M.J. Goin, M.T. Pearce, R.R. Dehoff, Strategy for Texture Management in Metals Additive Manufacturing, *Jom.* 69 (2017) 523–531. doi:10.1007/s11837-017-2264-3.
- [10] N. Raghavan, R. Dehoff, S. Pannala, S. Simunovic, M. Kirka, J. Turner, N. Carlson, S.S. Babu, Numerical modeling of heat-transfer and the influence of process parameters on tailoring the grain morphology of IN718 in electron beam additive manufacturing, *Acta Mater.* 112 (2016) 303–314. doi:10.1016/j.actamat.2016.03.063.
- [11] A. Rai, H. Helmer, C. Körner, Simulation of grain structure evolution during powder bed based additive manufacturing, *Addit. Manuf.* 13 (2016) 124–134. doi:10.1016/j.addma.2016.10.007.
- [12] M.R. Rolchigo, R. LeSar, Modeling of binary alloy solidification under conditions representative of Additive Manufacturing, *Comput. Mater. Sci.* 150 (2018) 535–545. doi:10.1016/j.commatsci.2018.04.004.
- [13] M. Tang, P.C. Pistorius, J.L. Beuth, Prediction of lack-of-fusion porosity for powder bed fusion, *Addit. Manuf.* 14 (2017) 39–48. doi:10.1016/j.addma.2016.12.001.
- [14] C. Weingarten, D. Buchbinder, N. Pirch, W. Meiners, K. Wissenbach, R. Poprawe, Formation and reduction of hydrogen porosity during selective laser melting of AlSi10Mg, *J. Mater. Process. Technol.* 221 (2015) 112–120. doi:10.1016/j.jmatprotec.2015.02.013.
- [15] A. Plotkowski, O. Rios, N. Sridharan, Z. Sims, K. Unocic, R. Ott, R. Dehoff, S.S. Babu, Evaluation of an Al-Ce alloy for laser additive manufacturing, *Acta Mater.* In Press (2016).
- [16] S.S. Babu, J.W. Elmer, J.M. Vitek, S.A. David, Time-resolved X-ray diffraction investigation of primary weld solidification in Fe-C-Al-Mn steel welds, *Acta Mater.* 50 (2002) 4763–4781. doi:10.1016/S1359-6454(02)00317-8.
- [17] P. Fernandez-Zelaia, S.N. Melkote, Process-structure-property modeling for severe plastic deformation processes using orientation imaging microscopy and data-driven techniques, *Integr.*

- Mater. Manuf. Innov. 8 (2019) 17–36.
- [18] E.A. Holm, R. Cohn, N.A.N. Gao, A.R. Kitahara, T.P. Matson, B.O. Lei, S.R.A.O. Yarasi, Overview : Computer Vision and Machine Learning for Microstructural Characterization and Analysis, Metall. Mater. Trans. A. 51 (2020) 5985–5999. doi:10.1007/s11661-020-06008-4.
- [19] M. Gaumann, C. Benzencon, P. Canalis, W. Kurz, Single-Crystal Laser Deposition of Superalloys Processing-Microstructure Maps, Acta Mater. 49 (2001) 1051–1062.
- [20] M. Haines, A. Plotkowski, C.L. Frederick, E.J. Schwalbach, S.S. Babu, A sensitivity analysis of the columnar-to-equiaxed transition for Ni-based superalloys in electron beam additive manufacturing, Comput. Mater. Sci. 155 (2018) 340–349. doi:10.1016/j.commatsci.2018.08.064.
- [21] T. Maeshima, Y. Kim, T.I. Zohdi, Particle-scale numerical modeling of thermo-mechanical phenomena for additive manufacturing using the material point method, Comput. Part. Mech. (2020). doi:10.1007/s40571-020-00358-x.
- [22] R. Komanduri, Z.B. Hou, Thermal analysis of the arc welding process: Part I. General solutions, Metall. Mater. Trans. B Process Metall. Mater. Process. Sci. 31 (2000) 1353–1370. doi:10.1007/s11663-000-0022-2.
- [23] M. Zavala-arredondo, H. Ali, K.M. Groom, K. Mumtaz, Investigating the melt pool properties and thermal effects of multi-laser diode area melting, Int. J. Adv. Manuf. Technol. (2018) 1383–1396.
- [24] J. Coleman, A. Plotkowski, B. Stump, N. Raghavan, A. Sabau, M.J.M. Krane, J. Heigel, R. Ricker, L. Levine, S.S. Babu, Sensitivity of Thermal Predictions to Uncertain Surface Tension Data in Laser Additive Manufacturing, J. Heat Transfer. 142 (2020).
- [25] G.A. Taylor, M. Hughes, N. Strusevich, K. Pericleous, Taylor_2002_Applied-Mathematical-Modelling, m (2002) 12.
- [26] R. Forslund, A. Snis, S. Larsson, Analytical solution for heat conduction due to a moving Gaussian heat flux with piecewise constant parameters, (2018). <http://arxiv.org/abs/1803.10668>.
- [27] B. Stump, A. Plotkowski, An adaptive integration scheme for heat conduction in additive manufacturing, Appl. Math. Model. 75 (2019) 787–805. doi:10.1016/j.apm.2019.07.008.
- [28] B. Stump, A. Plotkowski, A Forward Time Stepping Heat Conduction Model for Spot Melt Additive Manufacturing, 141 (2019). doi:10.1115/1.4044595.
- [29] B. Stump, A. Plotkowski, Spatiotemporal Parallelization of an Analytical Heat Conduction Model for Additive Manufacturing via a Hybrid OpenMP + MPI Approach, Comput. Mater. Sci. (2020).
- [30] F. Geiger, K. Kunze, T. Etter, Tailoring the texture of IN738LC processed by selective laser melting (SLM) by specific scanning strategies, Mater. Sci. Eng. A. 661 (2016) 240–246. doi:10.1016/j.msea.2016.03.036.
- [31] M. Ramsperger, C. Meid, D. Bu, Microstructure and Mechanical Properties of CMSX-4 Single Crystals Prepared by Additive Manufacturing, 49 (2018) 3781–3792. doi:10.1007/s11661-018-4762-5.
- [32] R. Shi, S. Khairallah, T. Roehling, T. Heo, J. McKeown, M. Matthews, Microstructural control in metal laser powder bed fusion additive manufacturing using laser beam shaping strategy, Acta Mater. 184 (2020) 284–305.
- [33] N. Raghavan, S. Simunovic, R. Dehoff, A. Plotkowski, J. Turner, M. Kirka, S. Babu, Acta Materialia Localized melt-scan strategy for site specific control of grain size and primary dendrite arm

- spacing in electron beam additive, *Acta Mater.* 140 (2017) 375–387. doi:10.1016/j.actamat.2017.08.038.
- [34] W. Halsey, J. Ferguson, A. Plotkowski, R. Deho, V. Paquit, Geometry-independent microstructure optimization for electron beam powder bed fusion additive manufacturing, 35 (2020). doi:10.1016/j.addma.2020.101354.
- [35] J.D. Hunt, Steady State Columnar and Equiaxed Growth of Dendrites and Eutectic, *Mater. Sci. Eng.* 65 (1984) 75–83.
- [36] N. Raghavan, B.C. Stump, P. Fernandez-Zelaia, M.M. Kirka, S. Simunovic, Influence of geometry on columnar to equiaxed transition during electron beam powder bed fusion of IN718, *Addit. Manuf.* 47 (2021) 102209. doi:10.1016/j.addma.2021.102209.
- [37] N.T. Nguyen, A. Ohta, K. Matsuoka, N. Suzuki, Y. Maeda, Analytical Solutions for Transient Temperature of Semi-Infinite Body Subjected to 3-D Moving Heat Sources, *Weld. Res. Suppl. I* (1999) 265–274.
- [38] C. Bishop, *Pattern Recognition and Machine Learning*, Springer, 2006.
- [39] C. Szegedy, W. Liu, Y. Jia, P. Sermanet, S. Reed, D. Anguelov, D. Erhan, V. Vanhoucke, A. Rabinovich, *Going Deeper with Convolutions*, (2014).
- [40] D.P. Kingma, Adam: A Method for Stochastic Optimization, *ICLR*. (2015) 1–15.
- [41] A. De Myttenaere, B. Golden, Mean Absolute Percentage Error for Regression Models, *Neurocomputing*. (2017).
- [42] B. Xu, N. Wang, T. Chen, M. Li, Empirical Evaluation of Rectified Activations in Convolutional Network, *ArXiv Prepr. ArXiv1505.00853*. (2015). <http://arxiv.org/abs/1505.00853>.
- [43] S.L. Smith, P. Kindermans, C. Ying, Q. V Le, G. Brain, Don't Decay the Learning Rate, Increase the Batch Size, *ICLR*. (2018) 1–11.
- [44] N. Raghavan, S. Simunovic, R. Dehoff, A. Plotkowski, J. Turner, M. Kirka, S. Babu, Localized melt-scan strategy for site specific control of grain size and primary dendrite arm spacing in electron beam additive manufacturing, *Acta Mater.* 140 (2017). doi:10.1016/j.actamat.2017.08.038.
- [45] B. Stump, A. Plotkowski, J. Coleman, Solidification Dynamics in Metal Additive Manufacturing: Analysis of Model Assumptions, *Model. Simul. Mater. Sci. Eng.* (2020).